CHEMNANOMAT

CHEMISTRY OF NANOMATERIALS FOR ENERGY, BIOLOGY AND MORE

Accepted Article

Title: Furan and Pyran Functional Groups Driven the Surface of Nitrogen-Doped Nanofiber Sponges

Authors: Juan L Fajardo-Diaz, Cristina L Rodriguez-Corvera, Emilio Munoz-Sandoval, and Florentino López-Urías

A Journal of

ACES
Asian Chemical
Editorial Society

A sister journal of **Chemistry – An Asian Journal** and **Asian Journal of Organic Chemistry**

WILEY-VCH

Furan and Pyran Functional Groups Driven the Surface of Nitrogen-Doped Nanofiber Sponges

M.Sc. Juan L. Fajardo-Díaz, M.Sc. Cristina L. Rodríguez-Corvera, Ph.D. Emilio Muñoz-Sandoval, Ph.D. Florentino López-Urías*

División de Materiales Avanzados, IPICYT, Camino a la Presa San José 2055, Lomas 4a sección, San Luis Potosí, S.L.P., 78216, México.

Abstract

Highly surface oxidized, nitrogen-doped, and nitrogen functionalized carbon nanotube sponge (N-CFS) were produced at 1020 °C using two sprayers approach in an aerosol-assisted chemical vapor deposition (AACVD) experiment. The structure of N-CFS consisted of entangled and corrugated carbon nanofibers of ~200 nm diameter, also showing junctions and knots. TEM characterizations revealed that the carbon nanofiber exhibits stacked graphitic layers in a transversal way with positive curvature. Superficial chemical analysis by XPS showed that the N-CFSs contain an atomic concentration of oxygen and nitrogen of 9.2 % and 2.9 %, respectively. The high-resolution XPS scans deconvolution-analysis revealed high percentages for C-O bonds, pyrrolic nitrogen doping, NH_3 functionalization, and Si-C interactions. The cyclic voltammetry measurements did not display a redox process despite the high oxygen concentration at the surface. Hydrophobic functional groups containing C-O bonds do not participate in a redox process (furan, pyran, epoxy, methoxy, ethoxy, among others) could mostly determine the electroactivity of N-CFS. Based on density functional theory calculations, we determine that the furans transfer a high amount of electron and promote a positive curvature in thin carbon nanotubes. Graphitic materials with furans, pyrans, and epoxy functional groups could be used as an anode in lithium-ion batteries.

*Correspondence address: flo@ipicyt.edu.mx

1. Introduction

A way to maintain the material properties of carbon nanostructures at the bulk level is using carbon allotropes as "building blocks" to create 3D carbon frameworks.[1–3] For example, using the single wall and multiwall carbon nanotubes[4,5], graphene intercalation,[6,7], and other combinations, several nanostructured architectures have been fabricated.[8,9] Dai et al.[10] created a carbon nanotube sponge using a pumped chemical vapor deposition (CVD) device and 1, 2-dichlorobenzene, ferrocene on a piece of quartz glass. They found that junctions between carbon nanostructures provide mechanical stability, elasticity, and excellent fatigue resistance. Luo et al.[11] synthesized well-aligned carbon nanotubes (CNT) by a two-step process. First, they produced the CNT by CVD, and subsequently, they mixed them with sodium dodecyl sulfate (SDS) in aqueous solution over sonication to create a CNT-SDS sponge via van der Waals interactions, this material exhibited a low density (< 50 mg/cm^{-3}), high porosity (>99.9 %) and high conductivity (~1.25 S/cm). He et al.[9] combined a melamine foam matrix impregnated with cobalt and iron solution in a CVD carbonization process to grow a hierarchical porous structure foam of nitrogen-doped CNT with a high capacitance performance. Regarding applications, three-dimensional carbon structures have been used in energy, medicine, material, and environmental sciences.[12,13] For example, Lu et al.[14] synthesized a hybrid sulfur/graphene carbon sponge with a high specific capacitance of 6.0 mAh/cm^2 at the first 11 cycles and stable capacity of 4.53 mAh/cm^2 after 300 cycles. Gui, et al.[15] developed a CNT-sponge with oil absorption capacities of 100 times its weight with the possibility of being used several times after a burning process without losing its absorption capacities.

Another issue for fabricating carbon-bulk nanostructures with exceptional electrical and chemical properties is the introduction of foreign atoms in the carbon network.[16,17] It is known that the incorporation of heteroatoms on the graphitic network induces structural and electronic transport changes. For example, phosphorous over the carbon network increase the surface area and the electrical density with potential application as a supercapacitor electrode.[18] Boron is used to inducing elbows, knees, and corrugated walls into carbon nanotubes and else increases the yield of high-oleophilic carbon nanotube sponges.[19,20] On the other hand, sulfur is used to create Y junctions has been reported that a carbon electrode sulfur and nitrogen co-doped increases the dynamic reaction and the cycling performance of LiS$_2$ batteries.[21,22] Furthermore, a high concentration of nitrogen promotes bends inwards the graphite layers and the formation of the "bamboo shape" structure.[16,23] Svintsiskiy et al.[24]

reported that the nitrogen in carbon nanotubes was at the internal arches as in the external surface of the graphitic wall, while for the nitrogen in platelet carbon nanofibers tend to be at the edges bending the graphitic layers. Additionally, nitrogen pyridinic and pyrrolic doping and amine functionalization on three-dimensional carbon nanostructures are used for the development of metal-free catalysts [25–27]. Recently, nitrogen-doped carbon sponges were synthesized using benzylamine as nitrogen source and ferrocene as a catalyst in an AACVD system (1020 °C) to be used as oil-recovery material with a superhydrophobic surface.[28] However, over the edge of non-saturated carbon atoms, nitrogen can be incorporated directly in a C-N bond or C-N-O bond. For example, the nitrogen can be found at the edges of carbon nanostructures built-in amines, amides, lactam, nitrogen oxides, pyridine-N-oxide, pyridinium, and hydrazone functional groups.[29–31]

In this work, we produce a high surface oxidized, nitrogen-doped, and nitrogen functionalized carbon nanotube sponge. We demonstrate that the use of pyridine and benzylamine can produce platelet-like graphitic carbon structure with amino and NOx nitrogen functionalities at the surface, and introduce pyrrolic doping and C≡N bonding. Despite the high oxygen concentration at the surface, no signals of the quinone/hydroquinone redox process were observed in cyclic voltammetry, which is confirmed by XPS, and FTIR characterization indicates mostly ether, ester, and aldehydes functionalizations. Interaction with Si from the quartz tube promotes the formation of Si clusters embedded over the graphitic structure. High charge capacity and ferromagnetic behavior were found. DFT simulation reveals that pyran and furan functionalities promote the formation of negatively charged regions in CNT, which could contribute to the development of Li-Ion batteries or molecular sensing.

2. Results and discussion

Figure 2 depicts the SEM images of the synthesized N-CFS material, where the overall configuration is constructed by entangled and interconnections of curved and robust carbon nanofibers. The junctions and knots are observed in figure 2a. Three types of morphologies were identified: i) branched and curved tubular carbon nanostructures with diameter of ~250 nm, where the entangled effect promotes in some cases the formation of junctions (red arrow); ii) thinner carbon fibers with diameter of ~120 nm producing complex knots (green arrow) and iii) the formation of spherical agglomerates of graphitic material (yellow arrow). More SEM images related to the N-CFS morphologies obtained can be observed in figure SI1-supplementary information. Figure 2b depicts

a magnification over one section of branched carbon fibers. Here is observed a cross-linked effect of carbon fiber with the formation "Y" and "+" junctions (red arrows). High magnification images reveal a rough appearance of the carbon nanofiber surface, see figures 2(c-d), which could be related to surface chemical speciation. EDX-SEM analysis over a section of the N-CFS reveals a global concentration of nitrogen of 4.33 wt.%, oxygen of 2.1 wt.%, and carbon of 93.5 wt.% (figure SI2-supplementary information). The cross-section of two carbon fibers is shown in figure 2c, where flat-type termination (blue arrow) and elliptical termination (red arrow) are observed. Also, Figure 2d shows the surface profile along the dashed line on the carbon fiber, revealing the valleys and elevations with a distance of ~85 nm between them (see the inset plot). Figure 2e also illustrates a transversal section of two fibers. It is possible to observe that the carbon nanofibers do no show inner tubular structure, but the structure shows broken graphitic sections probably related to a graphitic section surrounding the carbon nanofibers. The diameter of this carbon nanofiber is about 161.7 nm. Figure 2f depicts a histogram of the carbon nanofiber diameters. Two main sizes are possible to identify. One with sizes between 50 nm to 120 nm possible related to the thinner carbon nanofibers that produce knots. The second type has sizes between 120 nm to 300 nm with an average diameter of around 165 nm, very similar to the fiber shown in figure 2e. Most of the nanofiber falls on this diameter range.

The TEM image of carbon fibers showed a zigzagging behavior with a corrugated aspect, see blue and red arrows (figure 3a). Figure 3b displays the N-CFS with a highly deformed structure where protuberances are exhibited over the walls leading to bulky-smooth curves (red arrow) of sharp graphitic edges (blue arrow). Over the tip end of the N-CFS (Figure 3c), an unfolding effect is observed where the graphitic layers seem to be surrounding the structure similar to a graphite whisker structure[32]. The inset in figure 3c depicts a defined crystalline section embedded in the graphitic layer with an interlayer distance of 3.34 Å, presumably SiO_2 material as a consequence of interaction with the quartz tube. Figure 3d depicts two carbon fibers with irregular diameter, and high-stress sections are observed (red and green squares). Figure 3(e-h) illustrates the HRTEM images of the red and green squares. In figure 3d, the red box shows how the growing direction of the carbon fiber goes transversal to its axis, which indicates a "platelet-like" structure of carbon fiber [33]. In the case of the red box (figure 3e), homogeneous graphitic layers are observable; after an FFT treatment of the section, an interlayer distance of 3.6 Å was determined (figure 3f). Over the green box in figure 3g, the carbon fiber illustrates the transversal direction of the graphitic layers with an interlayer distance of 3.7 Å, lightly expanded considering the 3.45 interlayer distances for

multiwalled carbon nanotubes containing nitrogen[34]. Figure 3i shows a section of carbon fiber where two directions of the graphitic layers where observed. At the center, the graphitic layers go transversal to the growing axis while at the border, curved graphitic layers resembling a wrapping effect are observed (blue arrow). Figure 3j illustrates presumably iron-base catalytic nanoparticle of ~65 nm surrounded by ~8 nm of graphitic material. A smaller Fe-base nanoparticle (13 nm) seems to interrupt the longitudinal growth of graphitic layers (red arrow). By Z-contrast-TEM analysis over one carbon fiber (figure 3k), it is possible to observe that material with high atomic density is concentrated at the center of the carbon fiber. Nevertheless, the material is dispersed like elongated clusters embedded in graphitic layers (figure 3l). Energy-dispersive X-ray spectroscopy developed at the center of a carbon fiber reveals a high concentration of Si (figure SI3).

Figure 4a illustrates the X-ray diffraction pattern of the N-CFS material. A high-intensity peak identified at 26 degrees corresponds to the C (002) plane attributed to the graphitic structure. Also, a broad signal from 43 to 46 degrees was identified as iron compounds due to the formation of iron carbide (PDF 00-035-0772) and α-Fe (PDF 00-006-0696). A deconvolution analysis was developed over the C (002) plane using two pseudo-Voight curves[35] (figure 4b). Two signals were identified as γ-peak related to well-ordered graphitic layers at 26.1 degrees (3.41 Å), and π-peak related to the formation of turbostratic carbon at 25.4 degrees (3.48 Å), see table SI1. It is clear from XRD characterization that the N-CFS is mainly formed by a high oriented graphitic material (52.9 %) and a high concentration of turbostratic carbon (47.06 %). Nevertheless, to understand the nature of the graphitic structure, Raman spectroscopy was employed. Figure 4c shows the identified D-band, and G-band related to the breathing mode of the sp^2 C-C vibration due to structural defects and vacancies (1354 cm^{-1}) and the in-plane sp^2 C-C vibration mode (1584 cm^{-1}) respectively[36]. Also, second-order vibration modes were identified at 2667 cm^{-1} like 2D band related to the number of graphitic layers and the electronic configuration over the structure [36,37], in this case, the position of the 2D band shifted to the left could be related to a high electron concentration at the surface[37]- The D+D' band at 2896 cm^{-1} is related to a dispersion effect due to high defects formation[38]. A signal in 2133 cm^{-1} lightly visible could be related to the formation of graphynes type structures or alternated carbon-nitrogen lineal chains with C≡N bonds[39,40], possibly formed as a consequence due to the decomposition mechanism of pyridine. A deconvolution using Lorentz curves was developed over the D and G section using four peaks (figure 4d, table SI2) where the formation of a D* and a D** overtones are related to the influence of sp^3 C-C of amorphous carbon (1224 cm^{-1}) and the C-H influence over the edge of graphitic layers

(1496 cm^{-1})[41,42]. Additionally, the D** band can also be related to the effect of C-O functionalization over the C=C sp^2 bond on the graphitic structure[43]. The position of the D band and G band decreases (~15 cm^{-1}) to lower wavelengths compared with carbon nanotube sponge synthesized using benzylamine[44], this could be due to the presence of edges (D band) and high defects by bond disorder or owing to functionalization effects (G band)[45–47]. The I_D/I_G relation of 0.85 indicates a low defective graphitic carbon structure. [36]

Chemical surface features of the carbon fibers using XPS are shown in figure 5. The XPS survey revealed a high concentration of oxygen and nitrogen at the surface, reaching 9.2 wt./wt. % and 2.9 wt./wt. % respectively. Also, non-common incorporation of Si over the surface is observed (1.3 wt./wt. %). Figure 5b depicts the expanded high-resolution C1s peak. The C=C attributed to the graphitic structure, and the C-C due to the sp^3 aliphatic structures were deconvoluted. Besides, a considerable amount of the C at the surface related to the carbide formation (36 wt./wt. %) was detected. This fact could be related to the bond energies of Fe_3C formation (283.6 eV). Also, the interaction of carbon atoms with the Si (282.7 eV) is observables [48]. The formation of oxygen functionalities was identified with the energy formation of C-O (285.7 eV), C=O (286.5 eV), and COOH (287.4 eV)[49]. In the case of the C-N bond energy, this overlaps with the C-O energy vibration [50]. Figure 4c illustrates the deconvolution for the N1s region. A large amount of formation of the N-pyrrolic doping (N-5) is observed compared with N-pyridinic (N-6) and N-quaternary (N-Q). Furthermore, nitrogen functionalization is distinguished with energies corresponding to the amide, imine, and amide configuration (N3)[51,52], the pyridine-N-oxide (P-NOx), and the nitro (NOx) [53,54]. A signal below 398 eV is detected as N-Si binding energy possible due to the formation of C-Si interconnected graphitic materials [55]. In the case of the O1s section (figure 4d), the main contribution is observed over the C-O/COO– binding energies a part of hydroxyls, esters, amides, and anhydrides functionalities (532.1 eV) [56]. The presence of the FeO(OH) (530 eV) could be a consequence of the partial oxidation of external iron particles and Si-O bonds (533 eV) possible as part of a Si-O-CNT reaction[57]. More oxygen species were recognized as carbonyl functionalities (530.9 eV) and carboxylic functional groups (533.8 eV).

Figure 6a displays the FTIR spectra of N-CFS material. Signals were associated with the formation of the C-H$_x$ aliphatic structure, probably as part of an amine, ester, and ether functionalities by the doublet over ~2900 cm^{-1}.

The complement of the oxygen functional groups can be observed between 1650 cm^{-1} and 1850 cm^{-1}, where stretching vibrations due C=O configurations overlap and are related to the formation of carbonyl, carboxylic acid, quinone, pyrone, ester, and amides functionalities[50]. Also, the C-O vibration at ~1250 cm^{-1} is related to the formation of ester and ether chemical compounds, probably part of the structure as furans or pyrans and anchored to the graphitic structure on the surface. In the case of nitrogen vibration modes related to nitrogen species, those associated with the formation of amide and amine functionalities are appreciated near the ~3500 cm^{-1}. Also, the identification of a signal around 1645 cm^{-1} could be related to the formation of the amide structure. Geo et al.[47] indicate three significant peaks for amide structure anchored to MWCNT placed at 1639 cm^{-1} (O=C-N), 3320 cm^{-1} (N-H), and 2930/2852 cm^{-1} (-CH_2-/-CH_3) and a overshadow peak at 1565 cm^{-1} due to the C=C vibration mode associated with the incorporation of amide groups. Vibration modes related to the formation of nitrile structure and sp C≡C vibration mode nitriles and carbides were identified at ~2180 cm^{-1}, possibly associated with the light formation of graphyne structure[40]. Figure 6b schematize the different configuration that the oxygen and nitrogen atoms acquire for doping or functionalization. For oxygen, the functionalization of the graphitic structure can be achieved by the incorporation of amines, amides, imines, and the formation of the nitro group and Pyridine-N-oxide being these two, the more common[58]. TGA characterizations demonstrated that the sample is thermally stable (figure SI4), with a negligible loss of weight for T< 570 °C. At the end of the oxidation process at ~710 ºC can be observed that almost all the carbon structures were destroyed. The residual material contains sharped carbon edges and agglomerated pieces of the carbon materials.

Figure 7a illustrates the cyclic voltammetry curve at a rate of 10 mV/s. It is notable for the absence of the quinone oxide-reduction process due to the high surface oxygen content. This situation could be indicative that the main of the oxygen groups lay in the formation of ethers and ester functionalities. A light protuberance is observed over the -0.1V that can be related to the influence of nitrogen species like nitrogen doping and N-H functionalities like amines and amides in the oxidation process[59,60][61]. Figure 7b depicts the increase of the discharge rate (10 mV/s to 600 mV/s), showing a growth of capacity almost linear to the potential rate (not showed). A Coulombic efficiency determination technique was employed to determine the potential of the N-CFS material directly as an electrode for battery systems. Figure 7c shows the galvanostatic charge-discharge process over a potential of 1.1 V after several cycles (20 cycles) where after 500 s the time between lapses increases gradually. This behavior

can also be observed over the reversible charge-discharge changes in charge-capacity (Figure 7d). At the first stage (1 cycle), the current reaches the 0.011 mAh. However, after 20 cycles, the charge capacity increases to ~0.025 mAh. Figure 7e reveals the energy charge increases to its maxima after the 1375 s then stabilizes over 0.023 mWh. The Coulombic efficiency determined by the ratio between the charge capacity during discharge over the charge capacity during charge is shown in Figure 7f. The lowest efficiency value is reached in the 14 cycles (32 %); however, from this point, the efficiency tends to increase slightly to 34.4 % for the 20 cycles.

Figure 8a and Figure 8b illustrate the magnetization curve of the N-CFS structure with a coercive field of Hc = 245 Oe and saturation magnetization of Ms = 1.93 emu/g. This behavior could be compared to the hard ferromagnetic materials (Hc > 125 Oe)[62,63]. The saturation magnetization presents a value of 1.8 emu/g at ~0.5 T, which is comparable with the reported for pure CNT (Ms < 10 emu/g)[64]. Note that the reverse magnetization is probably by a coherent reversal mechanism, however at M=0, the direction of magnetization changes spontaneously. We did not find another magnetic material different from Fe_3C, but this behavior could be created due to the size of nanoparticles and the lack of magnetic material. Figure 8c displays the adsorption and desorption Brunner-Emmet-Teller (BET) isotherm. Due to the characteristic of the adsorption curve, this can be categorized as type IV typically associated with mesoporous carbon with a surface area (SA) of 8.6 m^2/g. The hysteresis could be considered as type H1 related to the bundle effect generated by the N-CFS structure. Figure 8d shows the Barrett-Joyner-Halenda (BJH) model to determinate the pore size distribution revealing that the mesoporosity domains over the macroporosity and no signals of microporosity is observed. The pore volume is 0.0278 cm3/g.

To determine the mechanical stability of the N-CFS structure, a compression test was developed. Figure 9a shows a photograph of the N-CFS material with a maximum length of approximately 4.5 cm and a thickness of 0.6 mm. Two cylinders with the diameter (0.6mm)-length proportions of 1:1 (figure 9b) and 1:2 (figure 9c) were obtained from the macroscopic N-CFS structure. Figure 9d illustrates the initial state of the compression process. At this point, the short cylinder is placed inside two metal discs with sufficient distance just to hold the N-CFS cylinder and without exerting any pressure over the sponge, in this case, 5.3 mm separation length (0 % strain). The final stage is considered when the material fractures after it is treated to a maximum stress load over its axial plane

(figure 9e). The minimal internal distance between the two metal discs is taken that changes from 5.3 mm to 1.9 mm. Figure 9f depicts the stress-strain curves for a large cylinder (red line) and a small cylinder (blue line). There are significant differences between the two samples. In the case of the large-cylinder, the maximum load reached before breaking is 54.2 MPa. This effect could be associated with a higher junction interaction of the carbon nanofibers, which increases its mechanical strength to stress. Yang et al. [65] reported how a 3D structure whit covalent junctions between graphitic structure and CNT withstands loads of 2.3 GPa. However, for the case of similar carbon sponge-type structures are reported to support around 60 kPa [10] or 100 kPa [4]. For the smaller cylinder, this support lower stress after breaking (6.1 MPa) but had higher compression support up to 63 % strain.

The decomposition temperature of pyridine (~680 °C)[66] and how the nitrogen is delivered from the molecule could be crucial to understand the effect of the different nitrogen-precursors on the structure of the carbon nanotubes. The decomposition mechanism of this precursor should be different since nitrogen in pyridine is found in an aromatic benzene-like ring, while in benzylamine, the nitrogen is found as an amine functional group (CH_2-NH_2) joined to a benzene ring. Ninomiya et al. [66] suggest that for pyridine decomposition, the less energetic state is the formation of cyanovinylacetylene ($^{\cdot}HC=CCH=CHC{\equiv}N$) radical, leading to the formation of minor fragments like of hydrogen cyanide, acetylene, and acrylonitrile. While, for the benzylamine decomposition, Song et al.[67] described that at high temperatures, the benzylamine leads to the formation of benzyl radical ($C_6H_5CH_2^{\cdot}$) and NH_2. It is expected that the pyridine favors the formation of N-quaternary and N-pyridinic since nitrogen is found in an aromatic benzene-like ring. In contrast, benzylamine should favor the creation of N-pyrrolic or nitrogen functionalities due to the amine functional group (CH_2-NH_2) joined to a benzene ring. In this case, the ethanol decomposition could give rise to the formation of $^{\cdot}CH_2OH$ and $^{\cdot}CH_3$ radicals[68].

From the results above presented, there is an intriguing situation concerning sponge surface composition and its electrochemical activity. On one side, the XPS characterizations showed a high oxygen concentration (9.2 %), while on the other side, the cyclic voltammetry characterizations do not show the redox process related to the quinone (C=O)/hydroquinone(C-OH) electron transfer process. Functional groups containing only C-O-C bonds does not participate in the redox process due to the oxygen atom can only form a maximal two sigma bonds. The high resolution deconvoluted O1s analysis showed that C-O bond concentration is over the other oxygen chemical

species, suggesting the presence of ether groups such as furans, pyrans, epoxy, methoxy, and ethoxy, among others. Notice that these groups have a hydrophobic feature, which could also explain the hydrophobic properties of N-CFS. To explain the role of these ether (C-O bonds) functional groups, we performed density-functional calculations considering different oxygen functional groups anchored on the surface of a graphene sheet[69]. The calculation method is described in Supplementary Information. Figure 10 displays the optimized structures of furans, pyrans, epoxy, methoxy, ethoxy, and ethyl-ester functional groups (electronic density of states can be seen in figure SI5). From Mulliken population analysis, the epoxy and furan functional groups pulled out 0.096 and 0.864 electrons, respectively, from the graphitic structure. Conversely, pyrans injected electrons (0.245 electrons). In both cases, electron-donating and withdrawing functional groups could create regions negatively charged, which could be anchoring sites for chemical species positively charged. Figure 11 shows the optimized structure of single-walled carbon nanotubes (SWCNT) with furan and pyran functional groups. We observed that the SWCNT(5,5) presents a positive curvature around the functional groups due to the pentagonal defects. Figure SI6 shows the electronic density of states plots. From Mulliken population analysis, the furan and pyran functional groups donate electrons to the carbon nanotube. The furans donate 0.546 and 0.305 electrons for SWCNTs (5,5) and (10,0), respectively. The pryans donate 0.170 and 0.217 electrons for SWCNTs (5,5) and (10,0), respectively. The presence of oxygens into the graphite lattice (furans and pyrans) may promote the existence of defects, principally vacancies, and curvature effects. Thus, the vacancies surrounded by oxygens negatively charged could be attractors of cations such as K^+, Na^+, and Li^+, among others.

3. Conclusions

We produced entangled nitrogen-doped carbon nanofiber sponges using an aerosol-assisted chemical vapor deposition method. The N-CFS material is formed by carbon fibers of around 200 nm diameter with a rough appearance, making junctions and knots. The main features exhibited by our N-CFS were: exhibited (1) high oxygen concentration, (2) nitrogen-doping and nitrogen-functionalization, (3) transversal graphite layer stacking, (4) Si interaction with CNF, (5) ferromagnetism at room temperature, and (6) electrochemical activity. The N-CFS exhibited a coercive field of 245 Oe, similar to that found in carbon nanotubes. The cyclic voltammetry did not show the quinone peak, suggesting that oxygen functionalities are more related to the ether, ester, and aldehydes structures, as also confirmed by XPS and FTIR characterizations. The magnitude of the oxidation and

reduction currents was higher than that found in carbon nanotubes produced by nitrogen precursors. DFT calculations showed that pyran and furans are structurally stable, which incorporates electrons to the graphite structures.

4. Experimental details

Nitrogen-doped and functionalized carbon nanofiber sponges (N-CFS) were synthesized by the AACVD technique. Figure 1 shows the approach which involves the pyrolysis using two different sprayers: i) sprayer A with an ethanol (C_2H_5OH), thiophene (C_4H_4S, 0.124 wt.%) and ferrocene ($Fe(C_5H_5)_2$ 1.252 wt.%) solution; ii) sprayer B with a 1:1 volume ratio of benzylamine ($C_6H_5CH_2NH_2$) and pyridine (C_5H_5N) solution mixed with thiophene (C_4H_4S, 0.5 wt.%) and ferrocene ($Fe(C_5H_5)_2$, 2.5 wt.%). The AACVD experiments were carried out at 1020 °C for 4 hours. In the case of the sprayer-A, an Ar gas with a flow of 0.8 l/min transported the cloud, and in the case of sprayer B, the gas carrier was a mixture of Ar-H_2 (95%-5%) with a flow of 1.0 l/min. The resulting material was collected from the reaction quartz tube by scraping and classified according to different zones in the quartz tube. Scanning and transmission electron microscopy characterizations (SEM and TEM) were used for morphological studies of the samples via a Helios Nanolab 600 Dual Beam and an FEI Tecnai F30, respectively. A Renishaw micro Raman spectrometer with a 532 nm excitation laser wavelength was used to evaluate the crystalline structure. The carbon, nitrogen, and oxygen content in the carbon N-CSTNs were measured by XPS (PHI 5000 VersaProbeII). Thermogravimetric analysis was performed using an STA 6000 Perkin-Elmer equipment in a temperature range of 50-950 °C with a heating speed of 10 °C /min under the dynamic flow of oxygen (20 ml/min). The magnetization saturation was measured by Dynacool equipment (Quantum Design) at 300 K. For the electrochemical properties, an Ag/AgCl electrode (0.197 V vs. NHE) was used as a reference electrode, and the N-CFS was used supported over a 916 stainless steel mesh to be as work electrode. The cyclic voltammetry was developed using an HCl 0.5 M solution as an electrolyte, with a potential window from -0.6 V to 1 V with variation in the scan rate from 10 mV/s to 400 mV/s.

Author contributions

EMS and FLU designed the research and wrote the manuscript. JLFD and CLRV conducted the experiments and analyzed the data.

Competing financial interests

Acknowledgments

References

[1]   A. Dasgupta, L. Pulickal, C. Rotella, Y. Lei, M. Terrones, Nano Today Covalent three-dimensional networks of graphene and carbon nanotubes : synthesis and environmental applications, Nano Today. 12 (2017) 116–135. https://doi.org/10.1016/j.nantod.2016.12.011.

[2]   A.L. Elías, N. Perea-López, L.P. Rajukumar, A. McCreary, F. López-Urías, H. Terrones, M. Terrones, Three-dimensional Nanotube Networks and a New Horizon of Applications, 2013. https://doi.org/10.1016/B978-1-4557-7863-8.00017-7.

[3]   J. Zhang, M. Terrones, C.R. Park, R. Mukherjee, M. Monthioux, N. Koratkar, Y.S. Kim, R. Hurt, E. Frackowiak, T. Enoki, Y.Y. Chen, Y.Y. Chen, A. Bianco, Carbon science in 2016: Status, challenges and perspectives, Carbon. 98 (2016) 708–732. https://doi.org/10.1016/j.carbon.2015.11.060.

[4]   C. Shan, W. Zhao, X.L. Lu, D.J. O'Brien, Y. Li, Z. Cao, A.L. Elias, R. Cruz-Silva, M. Terrones, B. Wei,

J. Suhr, Three-dimensional nitrogen-doped multiwall carbon nanotube sponges with tunable properties, Nano Letters. 13 (2013) 5514–5520. https://doi.org/10.1021/nl403109g.

[5]   S. Ozden, T. Tsafack, P.S. Owuor, Y. Li, A.S. Jalilov, R. Vajtai, C.S. Tiwary, J. Lou, J.M. Tour, A.D. Mohite, P.M. Ajayan, Chemically interconnected light-weight 3D-carbon nanotube solid network, Carbon. 119 (2017) 142–149. https://doi.org/10.1016/j.carbon.2017.03.086.

[6]   Z. Wu, S. Yang, Y. Sun, K. Parvez, X. Feng, 3D Nitrogen-Doped Graphene Aerogel-Supported Fe 3 O 4 Nanoparticles as Efficient Electrocatalysts for the Oxygen Reduction Reaction, Jacs. 134 (2012) 9082–9085. https://doi.org/10.1021/ja3030565.

[7]   L. Zhang, F. Zhang, X. Yang, G. Long, Y. Wu, T. Zhang, K. Leng, Y. Huang, Y. Ma, A. Yu, Y. Chen, Porous 3D graphene-based bulk materials with exceptional high surface area and excellent conductivity for supercapacitors, Sci Rep. 3 (2013) 1408. https://doi.org/10.1038/srep01408.

[8]   S. Vinod, C.S. Tiwary, L.D. Machado, S. Ozden, R. Vajtai, D.S. Galvao, P.M. Ajayan, Synthesis of ultralow density 3D graphene–CNT foams using a two-step method, Nanoscale. 8 (2016) 15857–15863. https://doi.org/10.1039/C6NR04252J.

[9]   S. He, H. Hou, W. Chen, 3D porous and ultralight carbon hybrid nanostructure fabricated from carbon foam covered by monolayer of nitrogen-doped carbon nanotubes for high performance supercapacitors, Journal of Power Sources. 280 (2015) 678–685. https://doi.org/10.1016/j.jpowsour.2015.01.159.

[10]   Z. Dai, L. Liu, X. Qi, J. Kuang, Y. Wei, H. Zhu, Z. Zhang, Three-dimensional Sponges with Super Mechanical Stability: Harnessing True Elasticity of Individual Carbon Nanotubes in Macroscopic Architectures., Scientific Reports. 6 (2016) 18930. https://doi.org/10.1038/srep18930.

[11]   S. Luo, Y. Luo, H. Wu, M. Li, L. Yan, K. Jiang, L. Liu, Q. Li, S. Fan, J. Wang, Self-assembly of 3D Carbon Nanotube Sponges: A Simple and Controllable Way to Build Macroscopic and Ultralight Porous Architectures, Advanced Materials. (2016) 1–8. https://doi.org/10.1002/adma.201603549.

[12]   X. Gui, J. Wei, K. Wang, A. Cao, H. Zhu, Y. Jia, Q. Shu, D. Wu, Carbon nanotube sponges, Advanced Materials. 22 (2010) 617–621. https://doi.org/10.1002/adma.200902986.

[13]   S. Nardecchia, D. Carriazo, M.L. Ferrer, M.C. Gutiérrez, F. del Monte, Three dimensional macroporous

Accepted Manuscript

architectures and aerogels built of carbon nanotubes and/or graphene: synthesis and applications., Chemical Society Reviews. 42 (2013) 794–830. https://doi.org/10.1039/c2cs35353a.

[14]   S. Lu, Y. Chen, X. Wu, Z. Wang, Y. Li, Three-dimensional sulfur/graphene multifunctional hybrid sponges for lithium-sulfur batteries with large areal mass loading, Scientific Reports. 4 (2014) 4–7. https://doi.org/10.1038/srep04629.

[15]   X. Gui, H. Li, K. Wang, J. Wei, Y. Jia, Z. Li, L. Fan, A. Cao, H. Zhu, D. Wu, Recyclable carbon nanotube sponges for oil absorption, Acta Materialia. 59 (2011) 4798–4804. https://doi.org/10.1016/j.actamat.2011.04.022.

[16]   P. Ayala, R. Arenal, M. Rümmeli, A. Rubio, T. Pichler, The doping of carbon nanotubes with nitrogen and their potential applications, Carbon. 48 (2010) 575–586. https://doi.org/10.1016/j.carbon.2009.10.009.

[17]   J. Park, M. Yan, Covalent functionalization of graphene with reactive intermediates, Accounts of Chemical Research. 46 (2013) 181–189. https://doi.org/10.1021/ar300172h.

[18]   J. Patiño, N. López-Salas, M.C. Gutiérrez, D. Carriazo, M.L. Ferrer, F. del Monte, Phosphorus-doped carbon–carbon nanotube hierarchical monoliths as true three-dimensional electrodes in supercapacitor cells, J. Mater. Chem. A. 4 (2016) 1251–1263. https://doi.org/10.1039/C5TA09210H.

[19]   D.P. Hashim, N.T. Narayanan, J.M. Romo-Herrera, D.A. Cullen, M.G. Hahm, P. Lezzi, J.R. Suttle, D. Kelkhoff, E. Muñoz-Sandoval, S. Ganguli, A.K. Roy, D.J. Smith, R. Vajtai, B.G. Sumpter, V. Meunier, H. Terrones, M. Terrones, P.M. Ajayan, Covalently bonded three-dimensional carbon nanotube solids via boron induced nanojunctions, Scientific Reports. 2 (2012) 1–8. https://doi.org/10.1038/srep00363.

[20]   A.A. Koós, F. Dillon, E.A. Obraztsova, A. Crossley, N. Grobert, Comparison of structural changes in nitrogen and boron-doped multi-walled carbon nanotubes, Carbon. 48 (2010) 3033–3041. https://doi.org/10.1016/j.carbon.2010.04.026.

[21]   J.M. Romo-Herrera, B.G. Sumpter, D.A. Cullen, H. Terrones, E. Cruz-Silva, D.J. Smith, V. Meunier, M. Terrones, An atomistic branching mechanism for carbon nanotubes: Sulfur as the triggering agent, Angewandte Chemie - International Edition. 47 (2008) 2948–2953.

https://doi.org/10.1002/anie.200705053.

[22] G. Zhou, E. Paek, G.S. Hwang, A. Manthiram, Long-life Li/polysulphide batteries with high sulphur loading enabled by lightweight three-dimensional nitrogen/sulphur-codoped graphene sponge, Nature Communications. 6 (2015) 1–11. https://doi.org/10.1038/ncomms8760.

[23] S.W. Pattinson, V. Ranganathan, H.K. Murakami, K.K.K. Koziol, A.H. Windle, Nitrogen-induced catalyst restructuring for epitaxial growth of multiwalled carbon nanotubes, ACS Nano. 6 (2012) 7723–7730. https://doi.org/10.1021/nn301517g.

[24] D.A. Svintsitskiy, L.S. Kibis, D.A. Smirnov, A.N. Suboch, O.A. Stonkus, O.Y. Podyacheva, A.I. Boronin, Z.R. Ismagilov, Spectroscopic study of nitrogen distribution in N-doped carbon nanotubes and nanofibers synthesized by catalytic ethylene-ammonia decomposition, Applied Surface Science. 435 (2018) 1273–1284. https://doi.org/10.1016/j.apsusc.2017.11.244.

[25] H. Wang, W. Wang, J. Key, S. Ji, Y. Ma, L. Khotseng, W. Lv, R. Wang, Sponge-like carbon containing nitrogen and iron provides a non-precious oxygen reduction catalyst, Journal of Solid State Electrochemistry. 19 (2015) 1181–1186. https://doi.org/10.1007/s10008-014-2719-1.

[26] S.S. Shinde, C.H. Lee, A. Sami, D.H. Kim, S.U. Lee, J.H. Lee, Scalable 3-D Carbon Nitride Sponge as an Efficient Metal-Free Bifunctional Oxygen Electrocatalyst for Rechargeable Zn-Air Batteries, ACS Nano. 11 (2017) 347–357. https://doi.org/10.1021/acsnano.6b05914.

[27] Y. Li, W. Liao, Z. Li, T. Feng, L. Sun, C. Guo, J. Zhang, J. Li, Building three-dimensional porous nano-network for the improvement of iron and nitrogen-doped carbon oxygen reduction electrocatalyst, Carbon. 125 (2017) 640–648. https://doi.org/10.1016/j.carbon.2017.09.106.

[28] E. Muñoz-Sandoval, J.L. Fajardo-Díaz, R. Sánchez-Salas, A.J. Cortés-López, F. López-Urías, Two Sprayer CVD Synthesis of Nitrogen-doped Carbon Sponge-type Nanomaterials, Scientific Reports. 8 (2018). https://doi.org/10.1038/s41598-018-20079-9.

[29] C. Zhang, R. Hao, H. Liao, Y. Hou, Synthesis of amino-functionalized graphene as metal-free catalyst and exploration of the roles of various nitrogen states in oxygen reduction reaction, Nano Energy. 2 (2013) 88–97. https://doi.org/10.1016/j.nanoen.2012.07.021.

[30] M. Seredych, D. Hulicova-Jurcakova, G.Q. Lu, T.J. Bandosz, Surface functional groups of carbons and the effects of their chemical character, density and accessibility to ions on electrochemical performance, Carbon. 46 (2008) 1475–1488. https://doi.org/10.1016/j.carbon.2008.06.027.

[31] K.A. Wepasnick, B.A. Smith, K.E. Schrote, H.K. Wilson, S.R. Diegelmann, D.H. Fairbrother, Surface and structural characterization of multi-walled carbon nanotubes following different oxidative treatments, Carbon. 49 (2011) 24–36. https://doi.org/10.1016/j.carbon.2010.08.034.

[32] M.S. Kim, Yoong Ahm; Hayashi, Takuya; Endo, Morinobu; Dresselhaus, Carbon Nanofibers, in: R. Vajtai (Ed.), Springer Handbook of Nanomaterials, Springer, Houston, TX, 2013: p. 1234. https://doi.org/10.1007/978-3-642-20595-8.

[33] R. Zheng, Y. Zhao, H. Liu, C. Liang, G. Cheng, Preparation, characterization and growth mechanism of platelet carbon nanofibers, Carbon. 44 (2006) 742–746. https://doi.org/10.1016/j.carbon.2005.09.015.

[34] C. Ducati, K. Koziol, S. Friedrichs, T.J. V Yates, M.S. Shaffer, P.A. Midgley, A.H. Windle, Crystallographic order in multi-walled carbon nanotubes synthesized in the presence of nitrogen, Small. 2 (2006) 774–784. https://doi.org/10.1002/smll.200500513.

[35] D.K. Singh, P.K. Iyer, P.K. Giri, Diameter dependence of interwall separation and strain in multiwalled carbon nanotubes probed by X-ray diffraction and Raman scattering studies, Diamond and Related Materials. 19 (2010) 1281–1288. https://doi.org/10.1016/j.diamond.2010.06.003.

[36] M.S. Dresselhaus, A. Jorio, M. Hofmann, G. Dresselhaus, R. Saito, Perspectives on carbon nanotubes and graphene Raman spectroscopy, Nano Letters. 10 (2010) 751–758. https://doi.org/10.1021/nl904286r.

[37] A. Das, S. Pisana, B. Chakraborty, S. Piscanec, S.K. Saha, U. V Waghmare, K.S. Novoselov, H.R. Krishnamurthy, A.K. Geim, A.C. Ferrari, A.K. Sood, Monitoring dopants by Raman scattering in an electrochemically top-gated graphene transistor, 3 (2008) 1–6. https://doi.org/10.1038/nnano.2008.67.

[38] A.C. Ferrari, D.M. Basko, Raman spectroscopy as a versatile tool for studying the properties of graphene, (2013) 1–13. https://doi.org/10.1038/nnano.2013.46.

[39] S. Zhang, J. Wang, Z. Li, R. Zhao, L. Tong, Z. Liu, Raman Spectra and Corresponding Strain Eff ects in Graphyne and Graphdiyne, (2016). https://doi.org/10.1021/acs.jpcc.5b12388.

[40]   M. Inagaki, F. Kang, Graphene derivatives: graphane, fluorographene, graphene oxide, graphyne and

graphdiyne, Journal of Materials Chemistry A: Materials for Energy and Sustainability. 2 (2014) 13193–

13206. https://doi.org/10.1039/C4TA01183J.

[41]   J. Schwan, S. Ulrich, V. Batori, H. Ehrhardt, S.R.P. Silva, Raman spectroscopy on amorphous carbon

films, Journal of Applied Physics. 80 (1996) 440–447. https://doi.org/10.1063/1.362745.

[42]   A. Kaniyoor, S. Ramaprabhu, A Raman spectroscopic investigation of graphite oxide derived graphene

A Raman spectroscopic investigation of graphite oxide derived graphene, 032183 (2014) 0–13.

https://doi.org/10.1063/1.4756995.

[43]   P. Vecera, J.C. Chacón-Torres, T. Pichler, S. Reich, H.R. Soni, A. Görling, K. Edelthalhammer, H.

Peterlik, F. Hauke, A. Hirsch, Precise determination of graphene functionalization by in situ Raman

spectroscopy, Nature Communications. 8 (2017). https://doi.org/10.1038/ncomms15192.

[44]   E. Muñoz-Sandoval, A.J. Cortes-López, B. Flores-Gómez, J.L. Fajardo-Díaz, R. Sánchez-Salas, F.

López-Urías, Carbon sponge-type nanostructures based on coaxial nitrogen-doped multiwalled carbon

nanotubes grown by CVD using benzylamine as precursor, Carbon. 115 (2017).

https://doi.org/10.1016/j.carbon.2017.01.010.

[45]   A.C. Ferrari, J. Robertson, Interpretation of Raman spectra of disordered and amorphous carbon,

Physical Review B. 61 (2000) 14095–14107. https://doi.org/10.1103/PhysRevB.61.14095.

[46]   C. Casiraghi, A. Hartschuh, H. Qian, S. Pliscanec, C. Georgia, A. Fasoli, K.S. Novoselov, D.M. Basko,

A.C. Ferrari, Raman spectroscopy of graphene edges, Nano Letters. 9 (2009) 1433–1441.

https://doi.org/10.1021/nl8032697.

[47]   C. Gao, Y.Z. Jin, H. Kong, R.L.D. Whitby, S.F.A. Acquah, G.Y. Chen, H. Qian, A. Hartschuh, S.R.P.

Silva, S. Henley, P. Fearon, H.W. Kroto, D.R.M. Walton, Polyurea-Functionalized Multiwalled Carbon

Nanotubes : Synthesis , Morphology , and Raman Spectroscopy, (2005) 11925–11932.

[48]   B.P. Swain, The analysis of carbon bonding environment in HWCVD deposited a-SiC:H films by XPS

and Raman spectroscopy, Surface and Coatings Technology. 201 (2006) 1589–1593.

https://doi.org/10.1016/j.surfcoat.2006.02.029.

[49]   H.R. Byon, B.M. Gallant, S.W. Lee, Y. Shao-Horn, Role of oxygen functional groups in carbon

nanotube/graphene freestanding electrodes for high performance lithium batteries, Advanced Functional

Materials. 23 (2013) 1037–1045. https://doi.org/10.1002/adfm.201200697.

[50]   J.L. Figueiredo, M.F.R. Pereira, The role of surface chemistry in catalysis with carbons, Catalysis Today.

150 (2010) 2–7. https://doi.org/10.1016/j.cattod.2009.04.010.

[51]   M.I. Ionescu, Y. Zhang, R. Li, H. Abou-Rachid, X. Sun, Nitrogen-doping effects on the growth, structure

and electrical performance of carbon nanotubes obtained by spray pyrolysis method, Applied Surface

Science. 258 (2012) 4563–4568. https://doi.org/10.1016/j.apsusc.2012.01.028.

[52]   K. Ghosh, M. Kumar, T. Maruyama, Y. Ando, Micro-structural, electron-spectroscopic and field-

emission studies of carbon nitride nanotubes grown from cage-like and linear carbon sources, Carbon. 47

(2009) 1565–1575. https://doi.org/10.1016/j.carbon.2009.02.007.

[53]   R. Arrigo, M. Hävecker, S. Wrabetz, R. Blume, M. Lerch, J. McGregor, E.P.J. Parrott, J.A. Zeitler, L.F.

Gladden, A. Knop-Gericke, R. Schlögl, D.S. Su, Tuning the acid/base properties of nanocarbons by

functionalization via amination, Journal of the American Chemical Society. 132 (2010) 9616–9630.

https://doi.org/10.1021/ja910169v.

[54]   R. Pietrzak, XPS study and physico-chemical properties of nitrogen-enriched microporous activated

carbon from high volatile bituminous coal, Fuel. 88 (2009) 1871–1877.

https://doi.org/10.1016/j.fuel.2009.04.017.

[55]   P. Mélinon, B. Masenelli, F. Tournus, A. Perez, Playing with carbon and silicon at the nanoscale, Nature

Materials. 6 (2007) 479–490. https://doi.org/10.1038/nmat1914.

[56]   Y.C. Chiang, W.H. Lin, Y.C. Chang, The influence of treatment duration on multi-walled carbon

nanotubes functionalized by H2SO4/HNO3 oxidation, Applied Surface Science. 257 (2011) 2401–2410.

https://doi.org/10.1016/j.apsusc.2010.09.110.

[57]   P.C. Ma, J.K. Kim, B.Z. Tang, Functionalization of carbon nanotubes using a silane coupling agent,

Carbon. 44 (2006) 3232–3238. https://doi.org/10.1016/j.carbon.2006.06.032.

[58]   R.J.J. Jansen, H. van Bekkum, XPS of nitrogen-containing functional groups on activated carbon,

Carbon. 33 (1995) 1021–1027. https://doi.org/10.1016/0008-6223(95)00030-H.

[59]   L. Lai, L. Chen, D. Zhan, L. Sun, J. Liu, S.H. Lim, C.K. Poh, Z. Shen, J. Lin, One-step synthesis of NH 2 -graphene from in situ graphene-oxide reduction and its improved electrochemical properties, Carbon. 49 (2011) 3250–3257. https://doi.org/10.1016/j.carbon.2011.03.051.

[60]   L. Lai, H. Yang, L. Wang, B.K. Teh, J. Zhong, H. Chou, L. Chen, W. Chen, Z. Shen, R.S. Ruoff, J. Lin, Preparation of supercapacitor electrodes through selection of graphene surface functionalities, ACS Nano. 6 (2012) 5941–5951. https://doi.org/10.1021/nn3008096.

[61]   C.L. Rodriguez-Corvera, J.L. Fajardo-Díaz, A.J. Cortés-López, L.E. Jiménez -Ramírez, E. Muñoz-Sandoval, F. López-Urías, Nitrogen-doped carbon fi ber sponges by using different nitrogen precursors : synthesis , characterization , and electrochemical activity, Materials Today Chemistry. 14 (2019) 1–13. https://doi.org/10.1016/j.mtchem.2019.100200.

[62]   G.E. Fish, Soft Magnetic Materials, 1990. https://doi.org/10.1109/5.56909.

[63]   J.M. Silveyra, E. Ferrara, D.L. Huber, T.C. Monson, Soft magnetic materials for a sustainable and electrified world, Science. 362 (2018). https://doi.org/10.1126/science.aao0195.

[64]   J. Su, Y. Gao, M. Sun, X. Han, X. Zhang, Q. Zhang, Fe- and Fe 3C-filled carbon nanotube-aligned arrays and flower-like carbon nanostructured clusters with a high coercivity, Micro and Nano Letters. 7 (2012) 271–274. https://doi.org/10.1049/mnl.2011.0597.

[65]   Y. Yang, N.D. Kim, V. Varshney, S. Sihn, Y. Li, A.K. Roy, J.M. Tour, J. Lou, In situ mechanical investigation of carbon nanotube–graphene junction in three-dimensional carbon nanostructures, Nanoscale. (2017) 2916–2924. https://doi.org/10.1039/C6NR09897E.

[66]   Y. Ninomiya, Z. Dong, Y. Suzuki, J. Koketsu, Theoretical study on the thermal decomposition of pyridine, Fuel. 79 (2000) 449–457. https://doi.org/10.1016/S0016-2361(99)00180-5.

[67]   S. Song, D.M. Golden, R.K. Hanson, C.T. Bowman, A shock tube study of benzylamine decomposition: Overall rate coefficient and heat of formation of the benzyl radical, Journal of Physical Chemistry A. 106 (2002) 6094–6098. https://doi.org/10.1021/jp020085l.

[68]   J. Li, A. Kazakov, F.L. Dryer, Experimental and numerical studies of ethanol decomposition reactions, Journal of Physical Chemistry A. 108 (2004) 7671–7680. https://doi.org/10.1021/jp0480302.

[69]   L.E. Jiménez-Ramírez, D.C. Camacho-Mojica, E. Muñoz-Sandoval, F. López-Urías, First-principles study of transition metal adsorbed on porphyrin-like motifs in pyrrolic nitrogen-doped carbon nanostructures, Carbon. 116 (2017) 381–390. https://doi.org/10.1016/j.carbon.2017.02.018.
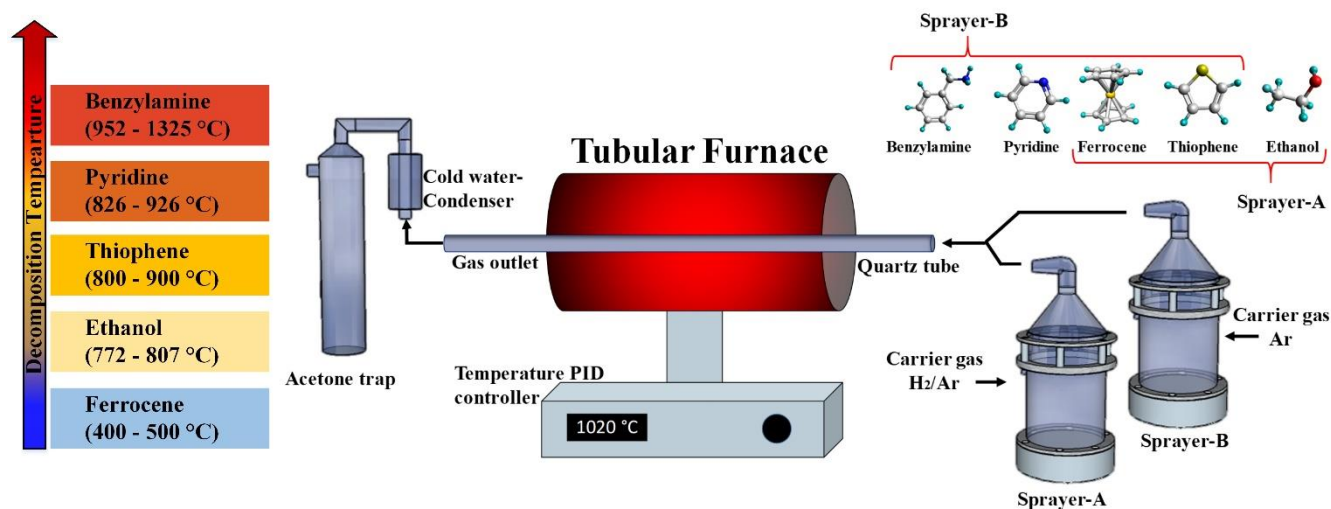
FIGURES AND CAPTIONS

Figure 1: Juan L. Fajardo-Diaz et al.

Figure 1: Schematic representation of a modified aerosol assisted chemical vapor deposition (AACVD) method used to synthesize the N-CFS materials. The AACVD arrangement consists of two independent sprayers feeding the reactor. The samples were synthesized at 1020 °C. The decomposition temperature ranges for the different precursors involved in the synthesis are also shown.

Figure 2: Juan L. Fajardo-Díaz et al.
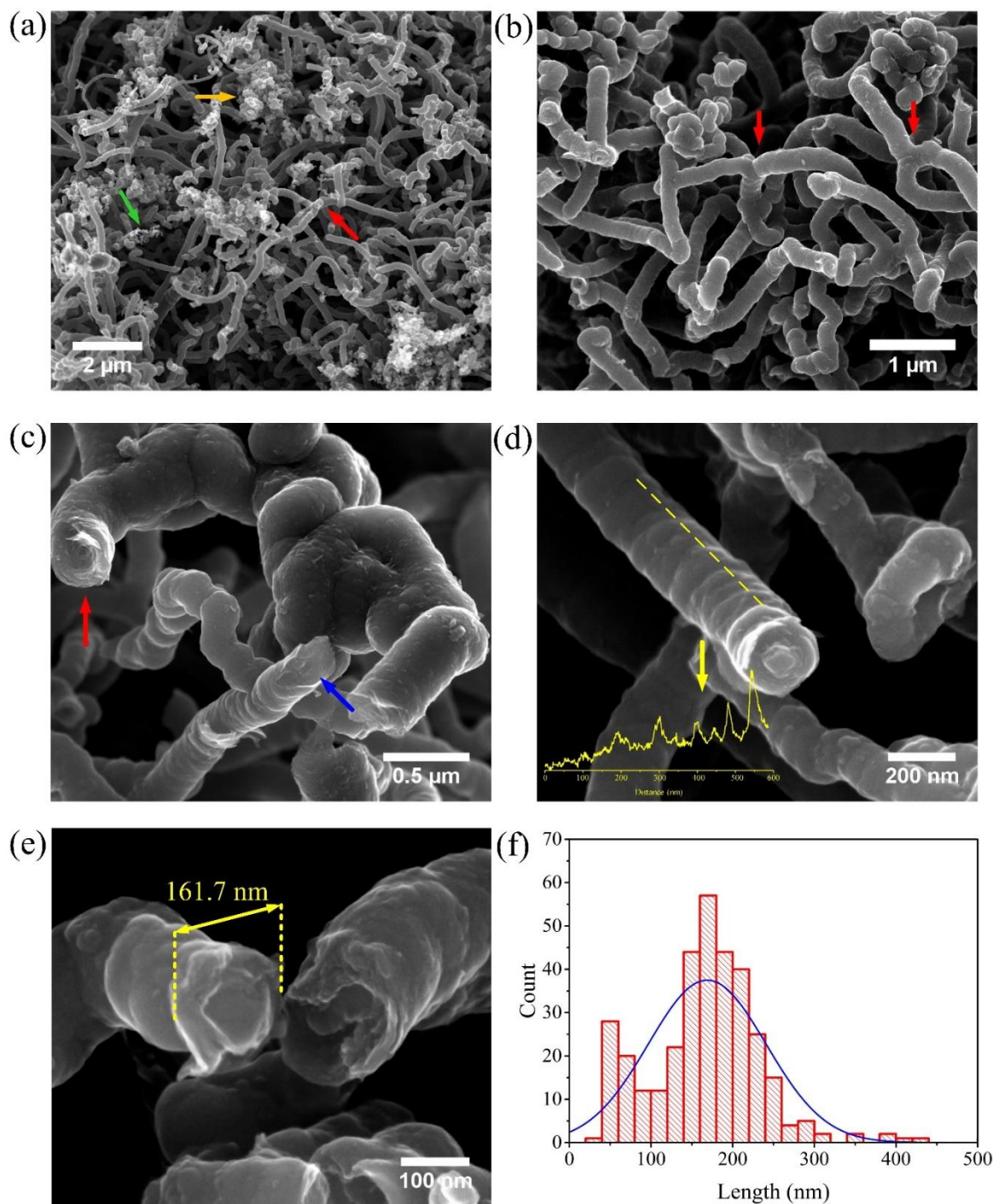
Figure 2: SEM images of carbon sponge material. **(a)** General view of the N-CFS where three morphologies are visible: curved tubular carbon nanostructures, curly carbon nanotubes, semi-spherical carbon aggregates. **(b)** Junctions between the carbon nanofibers (red arrow). **(c)** Cross-sections of the N-CFS with cylindrical geometry and unfolded graphitic structure (red arrow) and elliptical geometry (blue arrow). **(d)** Line-profile along the carbon fiber showing the surface reliefs. (e) High-magnification SEM over a transversal section of a CNF. **(f)** Diameter histogram showing an average diameter of 160 nm.

Figure 3: Juan L. Fajardo-Díaz et al.
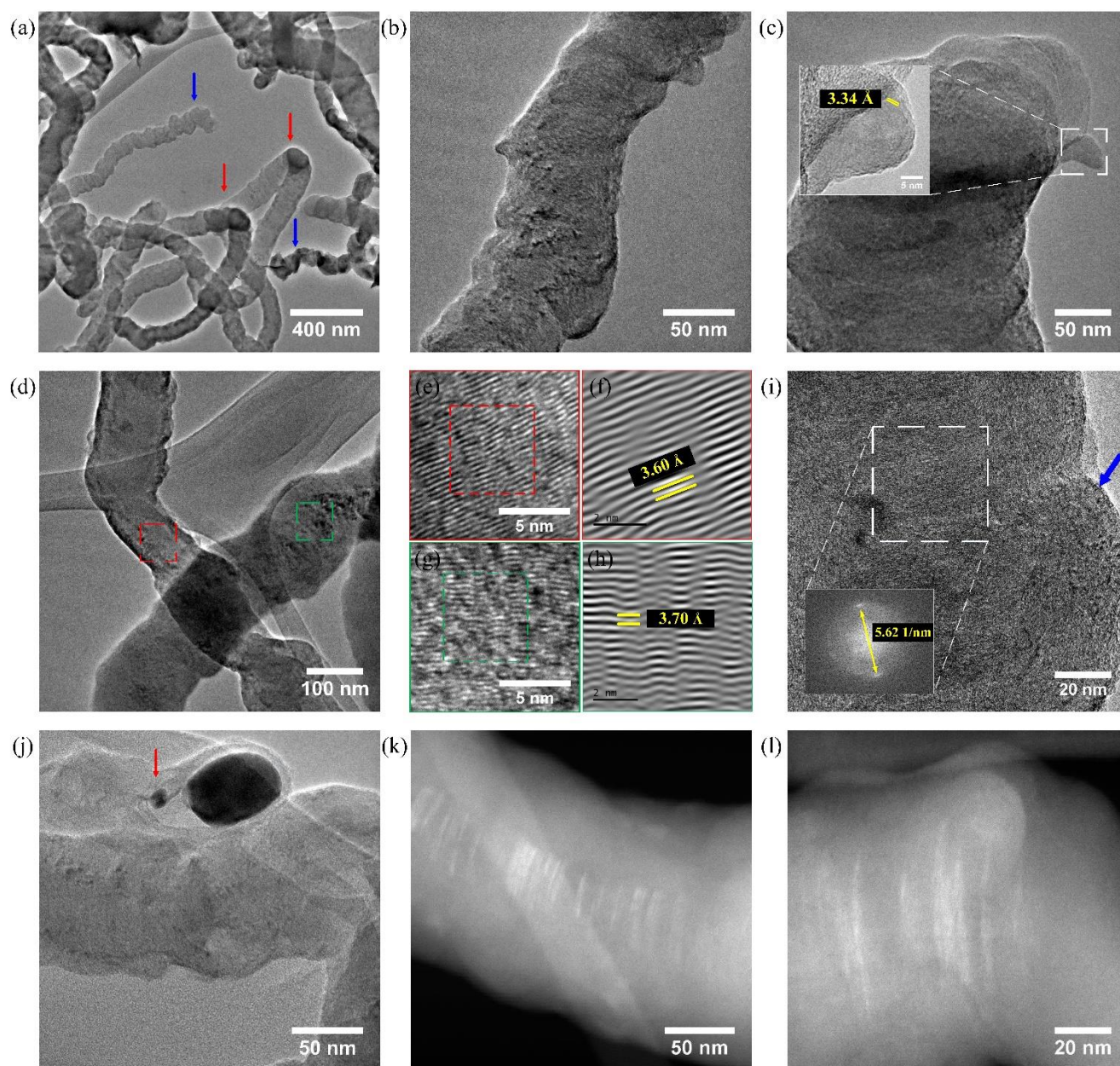
Figure 3: TEM and HRTEM images showing the different materials contained in the sample. **(a)** Typical carbon fiber structure part of the N-CFS structure. (b) Bulky CNF with surface irregularities. **(c)** Tip of a carbon fiber showing unfolded graphitic layers are observed; the inset shows a section of the graphitic material with an interlayer distance of 3.34 Å. **(d)** Carbon fiber, the red and green enclosed areas are analyzed in **(e-h)** by FFT refinement. **(i)** Borders and layered carbon fibers. **(j)** Iron nanoparticle (~65 nm) partially surrounded by graphitic material. **(k)** Z-contrast-TEM image over the main body of the CNF, where the bright spots indicate higher density material (Si). **(l)** An HR-Zeta contrast-TEM image where the material concentrates at the center of the CNF.
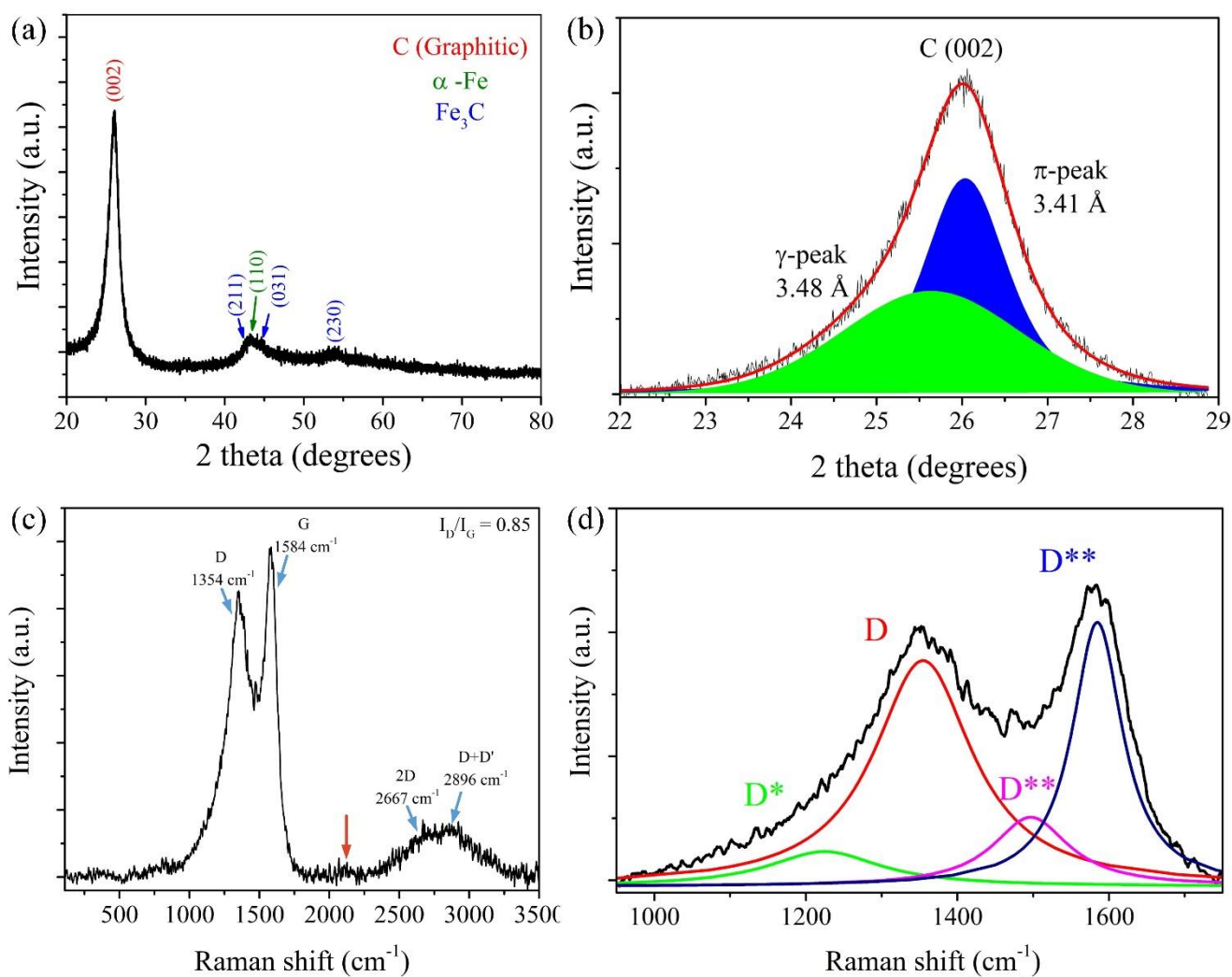
Figure 4: Juan L. Fajardo-Díaz et al.

Figure 4: (a) XRD diffraction pattern showing the C(002) peak attributed to graphitic material and signals associated with α-Fe (green), and Fe₃C (blue). **(b)** Deconvolution over the C (002) signal into two peaks: π-peak at 2θ = 26.1° related with the formation of well-aligned carbon nanostructure and the γ-peak at 2θ = 25.2° related with the formation of turbostratic graphene sheets and amorphous carbon. **(c)** Raman spectra from different synthesized samples using an excitation source of 533 nm (1.958 eV) laser. The D- band, and G-band for N-CFS at 1348 cm⁻¹ and 1582 cm⁻¹, respectively. The I_D/I_G ratio (0.87) indicates a less defective structure. **(d)** Deconvolution of Raman spectra using Lorentz fitting. Two more peaks are visible, the formation of D**-peak (1496 cm⁻¹) and D*-peak (1224 cm⁻¹) related to the influence in the sp² vibration modes by –sp³ C-H bonding, C-O bonding, and amorphous carbon.
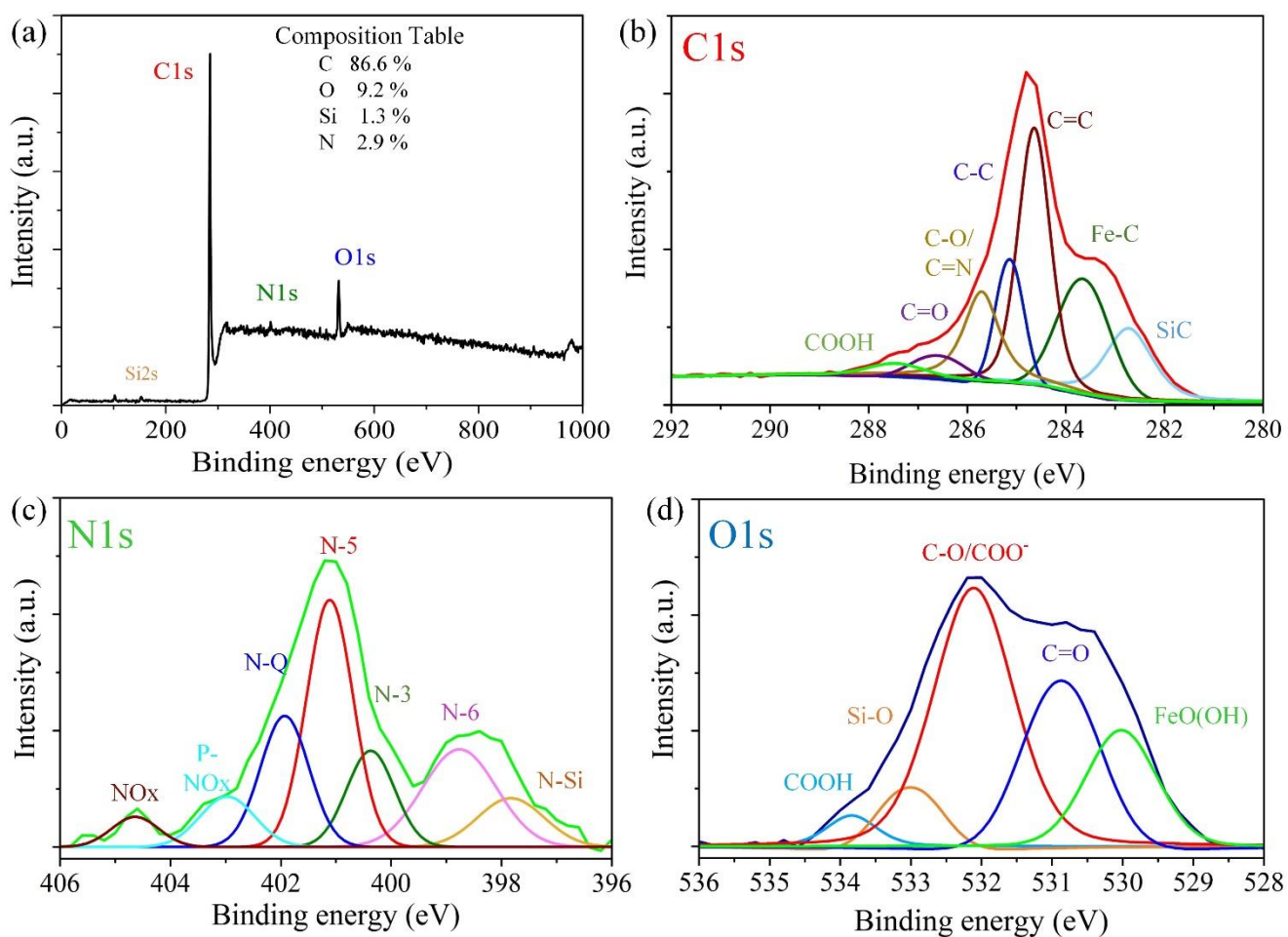
Figure 5: Juan L. Fajardo-Díaz et al.

Figure 5: (a) XPS survey scans revealing the presence of N, C, O, and Si. **(b-d)** Deconvoluted of the high-resolution XPS spectra. **(b)** C1s spectra showing the presence sp^2 hybridized carbons (C=C bonds), sp^3 hybridized carbons (C-C bond), and carbonyl C=O, and metal carbide compounds **(c)** O1s spectra showing the presence C=O, C-O, and Si-O bonds. **(d)** N1s spectrum revealing the presence of N-pyridinic (N-6), N-pyrrolic (N-5), N-quaternary (N-Q), and pyridine-oxide (P-NOx), and nitro structures over the surface (NOx), also the observation of nitrogen functionalities (N3) and N-Si bond. Deconvolution data such as binding energies, type of bond, FWHM, and integrated area can be seen in table SI3.
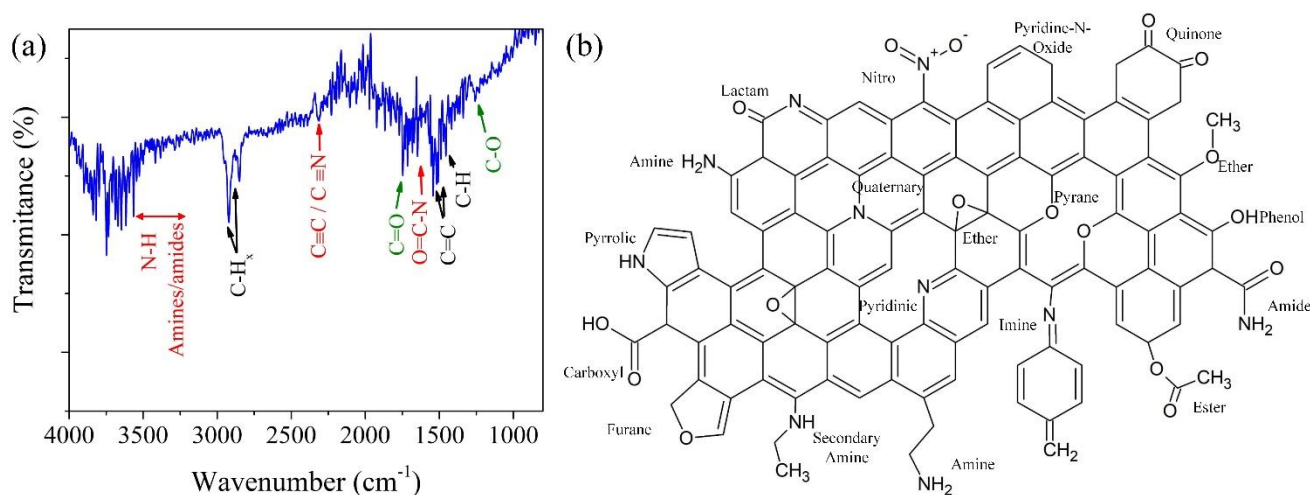
Figure 6: Juan L. Fajardo-Díaz et al.

Figure 6: (a) FTIR spectra revealed the presence of C-O and C=O (ketone, aldehyde, carboxylic acid, ester, and ether functionalities) and nitrogen bond related to the amine/amide functionalization, also a weak signal of cyanide bond vibration. **(b)** Schematic representation of oxygen and nitrogen functionalities in a graphene sheet, notice that most of the functional groups are at the edges.
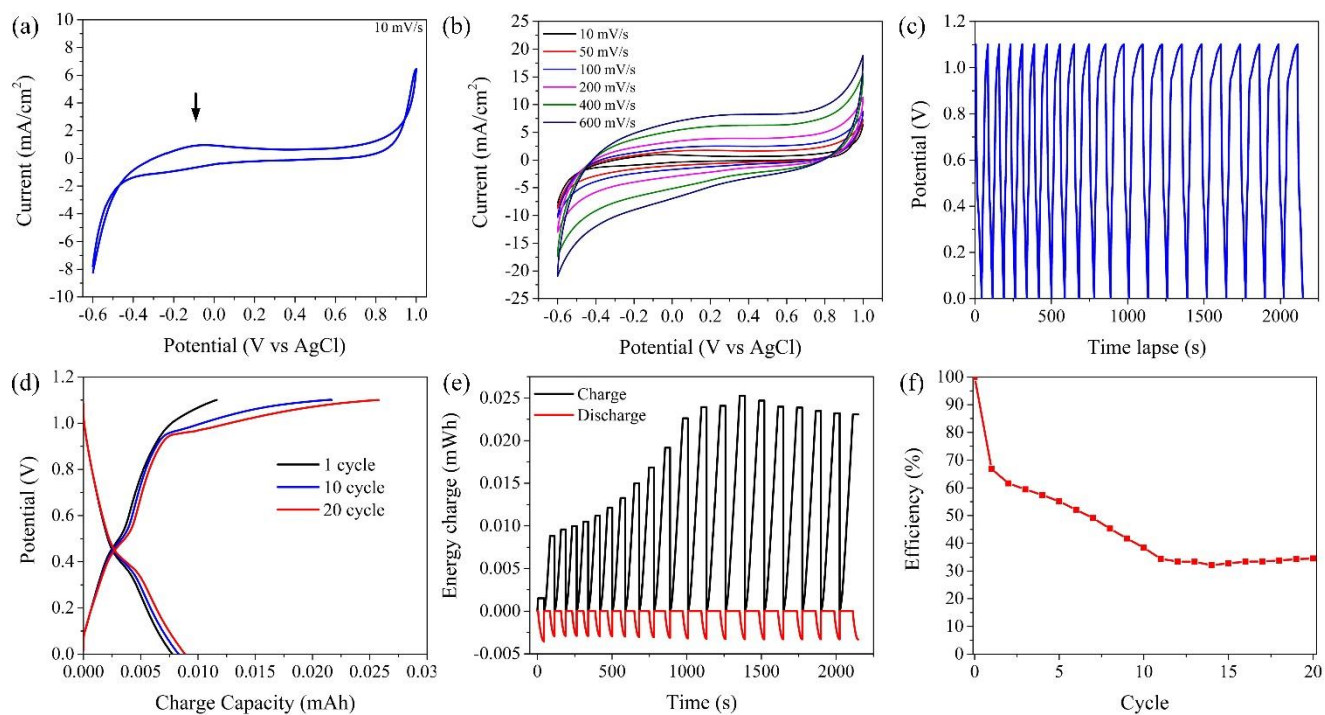
Figure 7: Juan L. Fajardo-Díaz et al.

Figure 7: (a) Cyclic voltammetry using a scan rate potential of 10 mV/s. **(b)** A charge capacity increase as the potential rate increases. **(c)** Galvanostatic charge-discharge process to 1.1V. **(d)** Reversible potential vs. charge capacity plot. **(e)** Energy charge process vs. cycle. **(f)** Coulombic efficiency plot.
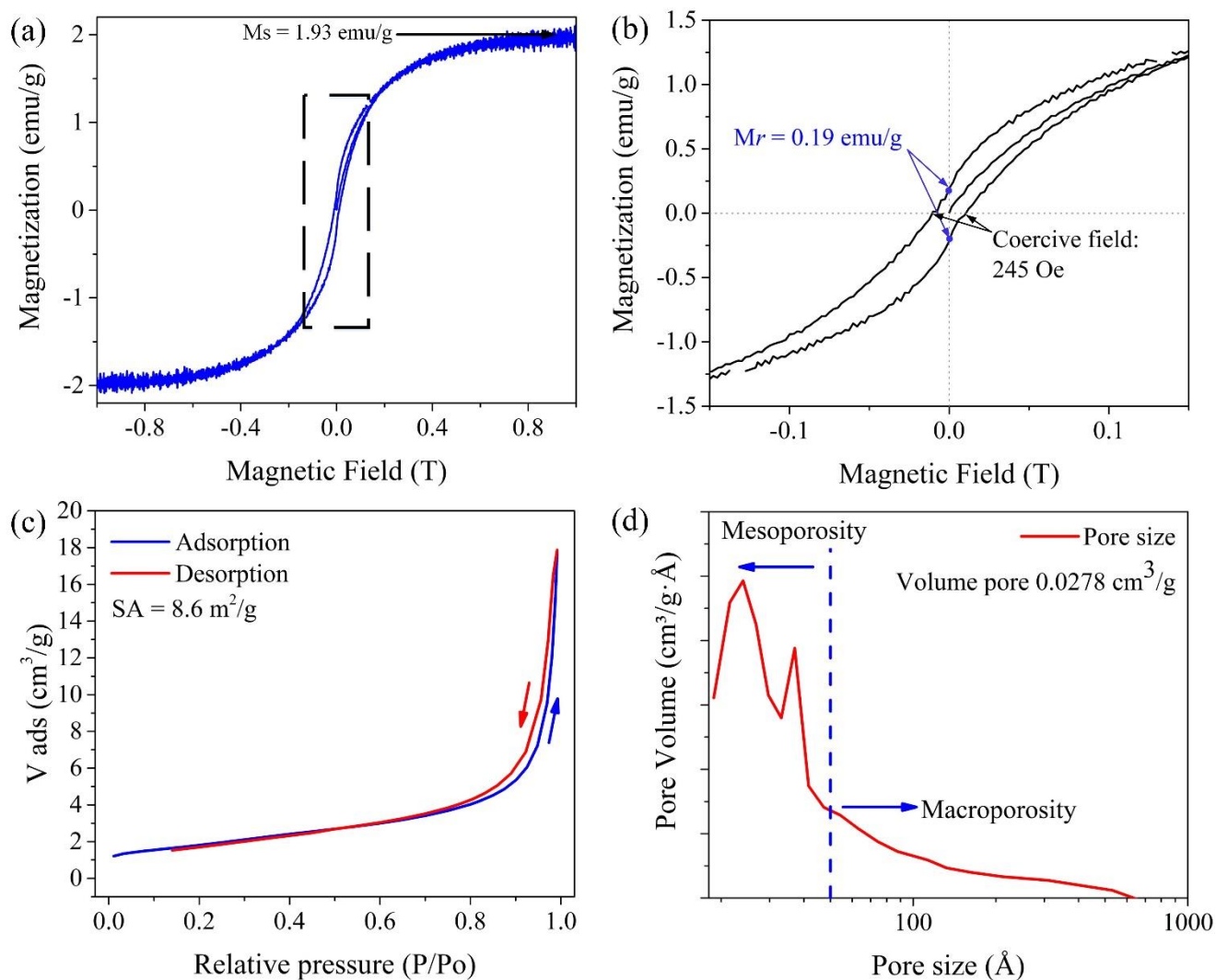
Figure 8: Juan L. Fajardo-Díaz et al.

Figure 8: (a) Magnetization curve of the N-CFS structure where saturation reaches the 1.93 emu/g. **(b)** Zoom over the magnetic hysteresis where the coercive field is 242 Oe. **(c)** N_2 adsorption-desorption isotherm for the N-CFS structure, where the behavior is related to a type IV isotherm with typeH1 hysteresis. **(d)** Pore size distribution where mainly mesoporosity is observed.
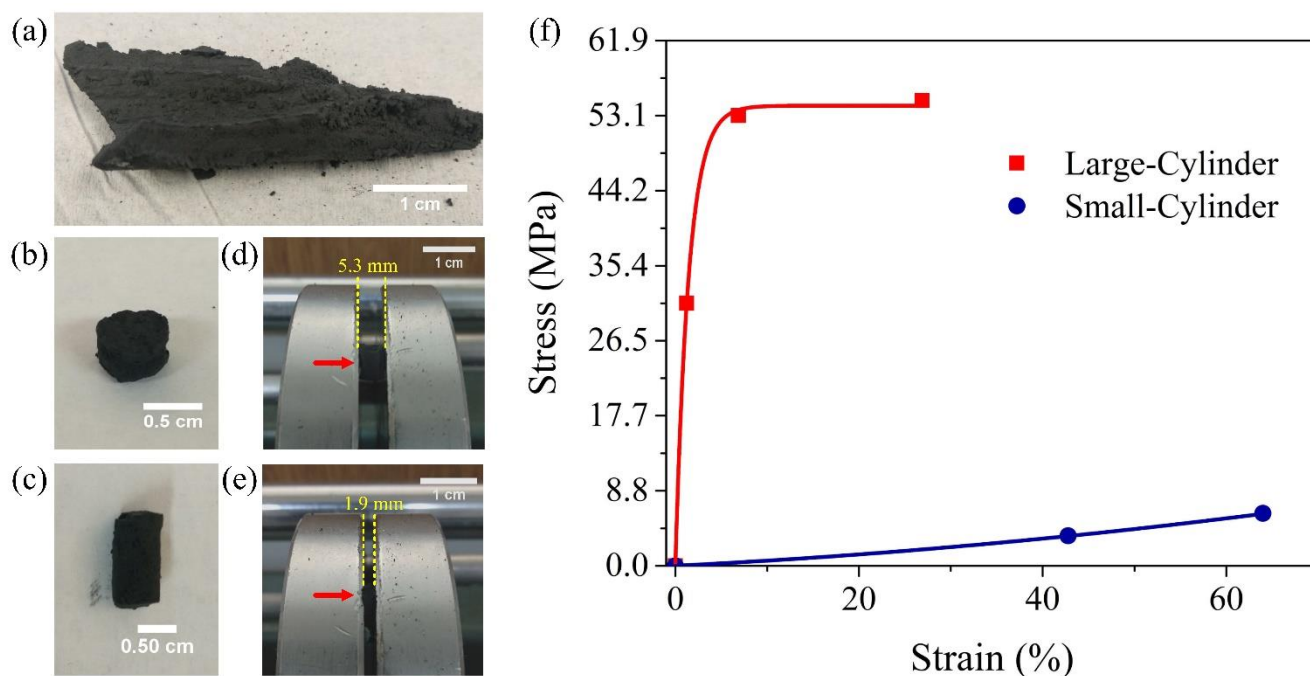
Figure 9: Juan L. Fajardo-Díaz et al.

Figure 9: (a) Photograph of the N-CFS macroscopic structure. **(b)** Small cylinder section with a diameter-length ratio of ~ 1:1 (6 mm). **(c)** Large cylinder section with a diameter-length ratio of 1:2. **(d)** Initial state at 0% load over the small cylinder. **(e)** Final state till break of the cylinder at maxima supported load. **(f)** Stress-strain curve for both cylinders.
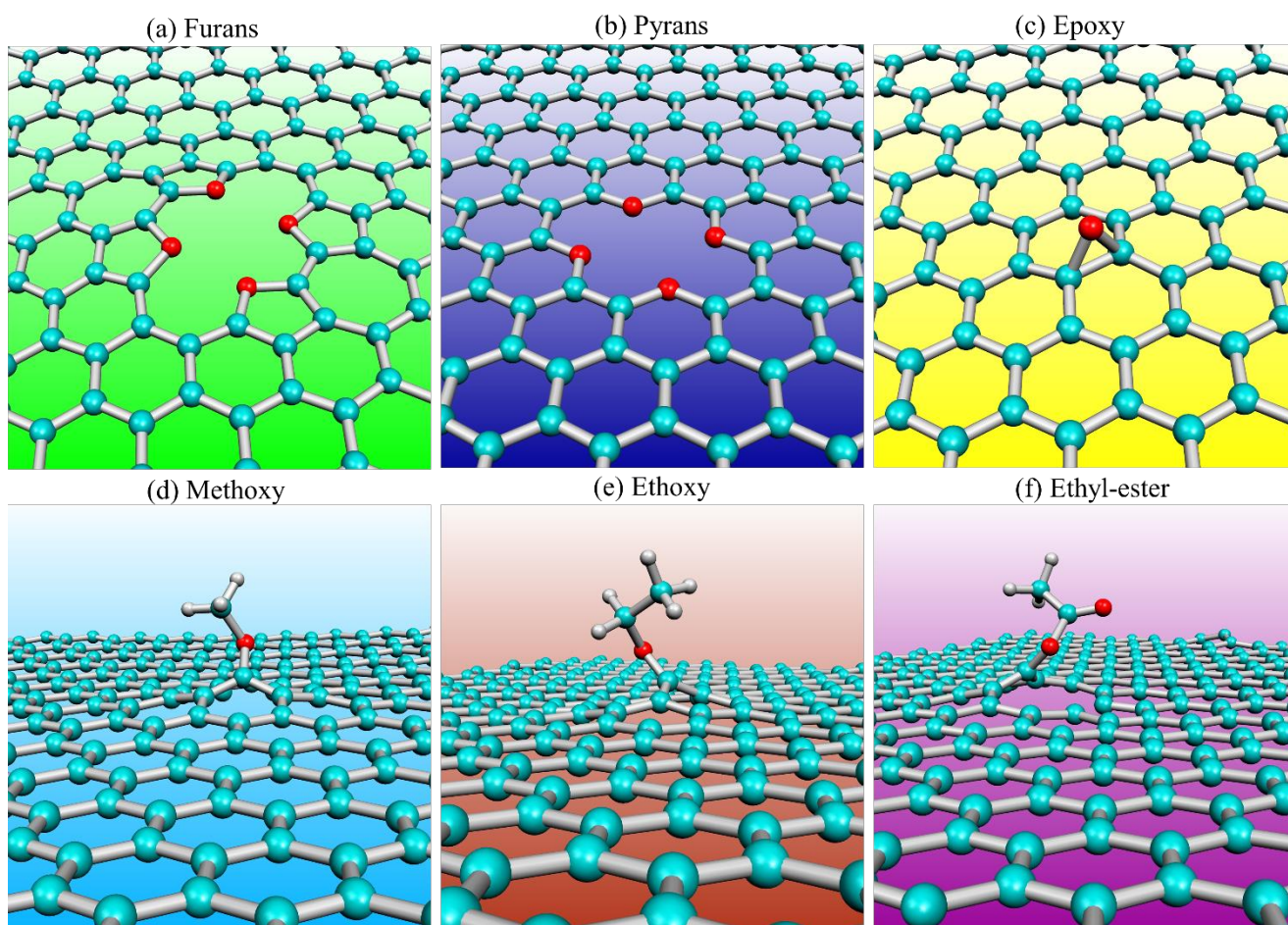
Figure 10: Juan L. Fajardo-Díaz et al.

(a) Furans   (b) Pyrans   (c) Epoxy

(d) Methoxy   (e) Ethoxy   (f) Ethyl-ester

Figure 10: Relaxed structure graphene sheet with different oxygen functional groups. **(a)** Furans (oxygen in pentagonal rings), more details on the creation of this defect is reported in Ref. [68]. **(b)** Pyrans (oxygen in hexagonal rings), here vacancies were generated into the graphitic lattice, and carbon doubly coordinated were replaced by oxygens. **(c)** Epoxy (oxygen adatom joined to two carbon atoms). **(d)** Methoxy with C-O bond. **(e)** Ethoxy with C-O bond. **(f)** Ethyl-ester with C-O and C=O bonds. In **(d-f)**, the functional groups were attached to a carbon atom surrounding a vacancy. The oxygen, carbon, and hydrogen atoms are set in red, cyan, and gray colors, respectively.
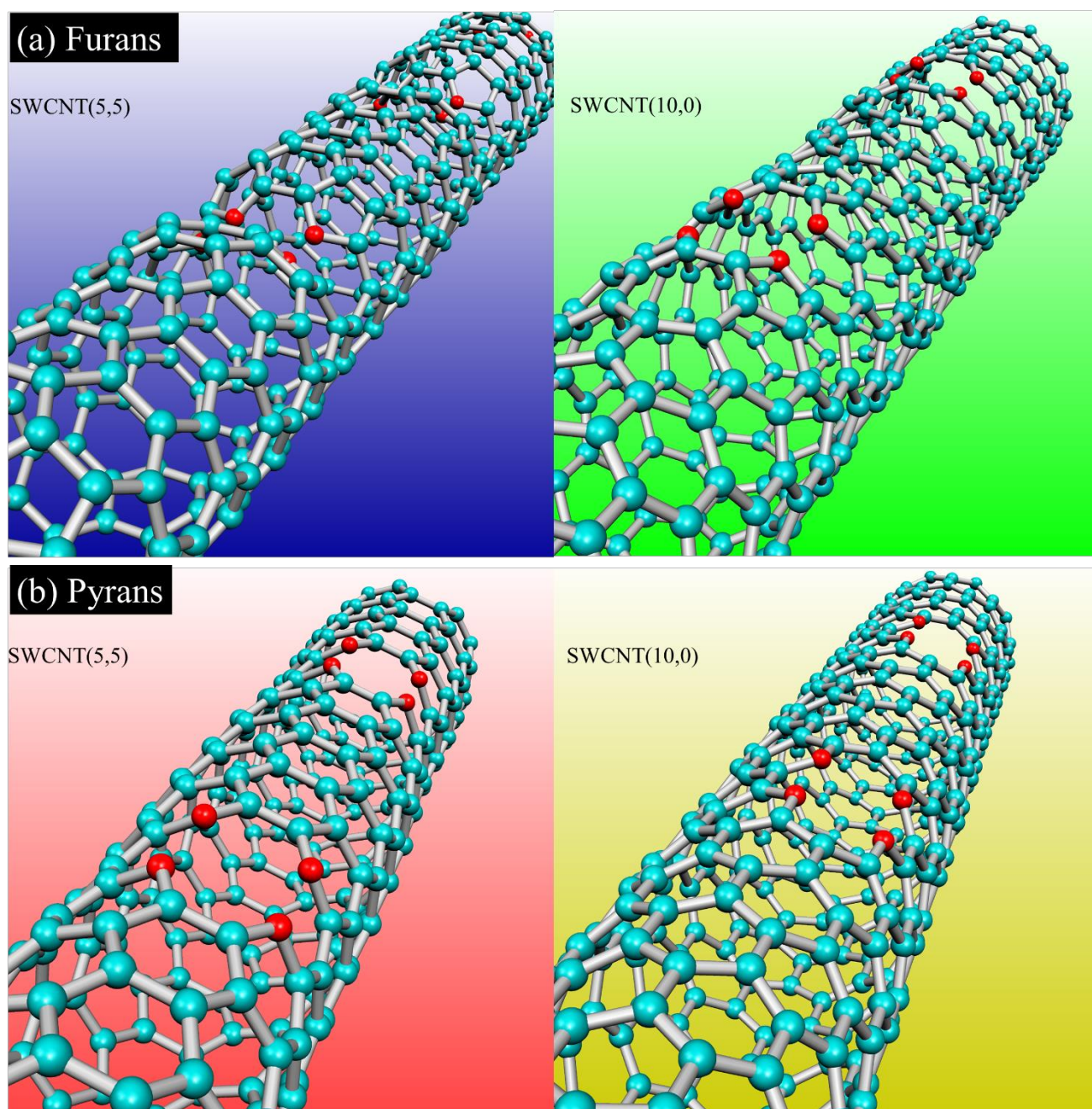
Figure 11: Juan L. Fajardo-Díaz et al.

Figure 11: Relaxed structure of single-walled carbon nanotubes containing **(a)** furan and **(b)** pyran functional groups. Results for SWCNTs (5,5) and (10,0). Notice that the SWCNT (5,5) with furan functional groups exhibit positive curvature.